The 20th International Conference on
Transport and Sedimentation of Solid Particles
26–29th September 2023, Wroclaw, Poland

ISSN 0867-7964 ISBN 978-83-7717-392-3

NUMERICAL INVESTIGATION OF PARTICLE TRANSPORT HYDRODYNAMICS INSIDE A WATER-IRON SAND JET

Ling XUE, Zuchao ZHU, Xianghui SU*

DOI: 10.30825/4.14-21.2023

Zhejiang Sci-Tech University, Hangzhou, China
e-mail: suxianghui@zstu.edu.cn

ABSTRACT: In order to investigate the mechanism of multi-phase jet technology with dense particles, the device used in cleaning steel strips was elected as the research object. The dynamics of jet flow and energy transfer in two-phase solid–liquid flow is extremely intricate. Constructing mathematical models of such interactions is challenging because of the complexity of particle-to-particle and particle-to-fluid contact. In this paper, an optimized method for considering a dense discrete-phase model is proposed to accurately track the movement of dense particles. Through this approach, the study is carried out in detail from the movement of particles, the corresponding mechanism of the flow field, and the characteristics of the wear. The results indicate that this method can calculate a large number of particles and capture their dynamics accurately. The particles obtain kinetic energy from the high-pressure jet, and most of them move downstream following the main flow. However, part of these solids migrated toward the bilateral region, created by the formation and evolution of the vortex which washes or scrubs the inside of the mixture chamber. These series of movement exhibit time-averaged characteristics in terms of the number of collisions, and the average normal and tangential forces. The curve of average wear rate ranges from a no wear stage, through rapid wear stage, to a rapid and stable stage according to the inner movement of solid-liquid flows.

KEYWORDS: numerical simulation, particle movement, solid-liquid two phase flow

1. INTRODUCTION

Abrasive water jet technology（AWJ）is a kind of surface treatment method widely used in polishing, grinding, cutting and other industries, where it uses nozzles to generate high velocity fluid with significant concentration of solid particles and direct the particles to impact the surface of a target, e.g., a corroded steel belt to remove impurities. Compared with the traditional pickling and manual process, this method is more controllable in terms of the degree of impurity removal, surface roughness and other technical indicators, and performs well in terms of energy conservation, environmental protection, removal efficiency and minimizing waste water discharge. The working principle of abrasive water jet nozzles is that the feeding high pressure fluid flows through the nozzles to generate the high velocity, which in turn generates a low-pressure region, inducing the abrasive slurry into the jet domain. Finally, the initial pressure of the working fluid is converted into the kinetic energy of the dense solid-liquid two-phase flow. The core unit of this device is the

solid-liquid two phase flow nozzle shown in Fig.1, the inlet for the working fluid is in the top, the transported media is in the left, then the mixed flow in the right.

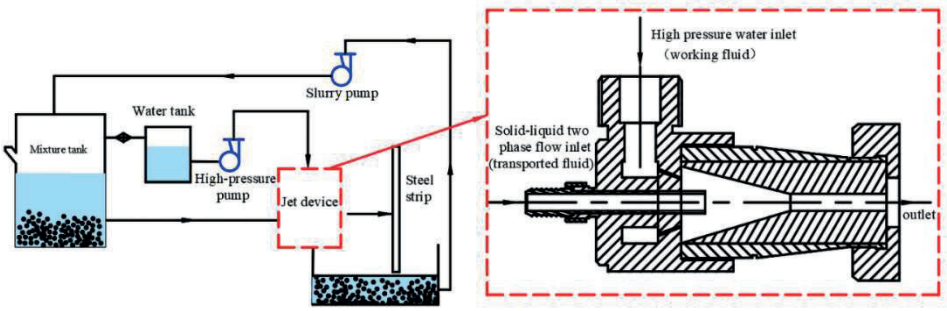

Fig.1 The typical nozzle structure of solid-liquid two-phase flow

In the application of abrasive water jets for polishing and cleaning, there are still some technical challenges, such as unsatisfactory solid-liquid mixture effect and serious wear of nozzle and threaten on lifetime. In order to solve these problems, it is important to explore the mechanism of dense solid-liquid two-phase flow in this complex environment. Although it is difficult to detect the migration of a huge amount of particles by experimental measurement, the significant progress in high-performance calculations and numerical algorithms make it possible to obtain informed insight into such flows. More and more reliable numerical simulations have been performed to investigate the migration phenomenon of particle and fluid coupling phenomena. The related researches mainly cover scientific issues on solid-liquid theoretical model, particle dynamics and the relationship between the internal flow and external performances.

Various numerical strategies are used to build particle-water models for studying this kind of solid-liquid flow inside the specific domains like nozzles. The Eulerian–Eulerian and Eulerian–Lagrangian methods are the two dominating approaches. In the framework of Eulerian–Eulerian, both solid particles and liquid are treated as a continuous phase, the two-phase flow then becomes the mixture and diffusion of two fluids. The main disadvantage of the Eulerian–Eulerian approach is that it takes a relatively long calculation time to evaluate the time-averaged solution. Instead of the Eulerian–Eulerian approach of assuming that the particles constitute a fluid phase, they are treated as discrete particles in the Eulerian-Lagrangian approach. The dynamic characteristics of the particles are governed by the particle motion equation (Newton′s second law) while the fluid flow is governed by the Navier-Stokes equation. Then the coupling between fluid flow field and particles' movement is solved to obtain the overall two-phase flow characteristics. Hence, this method can describe the movement of particles and their interaction in the flow field more accurately. Because of the above advantages, this method has been widely used in the research of pipeline pneumatic conveying, fluidized bed, cyclone separator and solid-liquid two-phase flow pump shown as Table 1. The Eulerian–Lagrangian method is divided into discrete phase method (DPM)and discrete element method (DEM). In the

DDPM, the kinetic theory of granular flow is adopted to calculate the particle interaction in the Eulerian frame of reference. This interaction is then mapped to the particles in the Lagrangian frame of reference. Whereas, CFD-DEM is only suitable for working conditions with small volume concentration, it ignores the volume effect of particles and the influence of the convection field. In view of the unclear mixing and injection mechanism of dense particle multiphased flow in finite space, the coupled DDPM model and DEM model are utilized here to simulate the solid-liquid two-phase flow with dense particle in nozzle in this work. We intend to combine the external performance and internal mechanism together to investigate the migration characteristics of dense particles and particle impact on the wall.

Table 1

Summary of the literature works showing the comparison between the Eulerian–Eulerian and Eulerian–Lagrangian approaches

Reference	Modeling approach	Sensitivity parameters investigated
Li et al	Eulerian-Eulerian	investigated the gas-solid hydrodynamics
Patro et al		simulated the sparse and turbulent gas-solid two-phase flow in vertical pipes
Shi et al		obtained understanding of the particle concentration
Adamczyk et al	Eulerian–Lagrangian	predicted particle transport in fluidized beds
Wu et al		simulated the complex gas–solid reacting flow

2. MATHEMATIC AND GEOMETRY MODEL

A. Solid-liquid model of dense particles

The basic idea of DDPM is to calculate the local properties of the particles from the equations of motion on the Lagrangian grid, and then interpolate them back to the Euler grid to calculate the average solid velocity and volume fraction.

$$\frac{\partial}{\partial_t}(\varepsilon_f \rho_f) + \nabla.(\varepsilon_f \rho_f \nu_f) = 0 \frac{\partial}{\partial_t}\left(\varepsilon_f \rho_f\right) + \nabla.\left(\varepsilon_f \rho_f \nu_f\right) = 0 \quad (1)$$

$$\frac{\partial}{\partial_t}\left(\varepsilon_f \rho_f \nu_f\right) + \nabla.\left(\varepsilon_f \rho_f \nu_f \nu_f\right) = -\varepsilon_f \nabla \mathrm{P} + \nabla.\tau_f + \varepsilon_f \rho_f g + K_{DPM}\left(\nu_p - \nu_f\right) + S_{DPM} \frac{\partial}{\partial_t}(\varepsilon_f \rho_f \nu_f) + \nabla.(\varepsilon_f \rho_f \nu_f \nu_f) = -\varepsilon_f \nabla \mathrm{P} + \nabla.\tau_f + \varepsilon_f \rho_f g + \mathrm{K_{DPM}}\left(\nu_p - \nu_f\right) + \mathrm{S_{DPM}} \quad (2)$$

where K_{DPM} represents the coefficient of the interphase exchange of momentum, ν_p is the average velocity of the particles, and S_{DPM} is the motion-dependent source term. The subscript "*f*" means the item of fluid and "*p*" represents that of particles.

The equation of particle motion in the solid phase is derived from the following formula by considering the force due to the liquid phase on these particles:

$$\frac{\mathrm{dv_p}}{\mathrm{dt}} = \mathrm{F_D}\left(\mathrm{v_f} - \mathrm{v_p}\right) + \frac{\mathrm{g}(\rho_\mathrm{p} - \rho_\mathrm{f})}{\rho_\mathrm{p}} + \mathrm{F_c}\,\frac{dv_p}{dt} = F_D\left(v_f - v_p\right) + \frac{g(\rho_p - \rho_f)}{\rho_p} + F_c \quad (3)$$

$$\frac{\mathrm{d}}{\mathrm{dt}}\mathrm{I_i}\omega_\mathrm{i} = \sum\nolimits_\mathrm{j}\left(\mathrm{r_i} \times \mathrm{F_{\tau,ij}} + \mathrm{M_i}\right)\frac{d}{dt}I_i\omega_i = \sum\nolimits_j\left(r_i \times F_{\tau,ij} + M_i\right) \quad (4)$$

where $F_D\left(v_f - v_p\right)$ is the acceleration due to the drag force, $\frac{g(\rho_p - \rho_f)}{\rho_p}$ is the acceleration due to gravity and F_c represent the acceleration due to particle collisions. w_i and I_i represent the angle velocity and Moment of inertia of particle i, respectively. M_i is the rolling friction torque of particle i and $F_{\tau,ij}$ is the stress contact force. The acceleration due to the drag force $F_D\left(v_f - v_p\right)$ can be defined as follows:

$$F_D\left(v_f - v_p\right) = \frac{3}{4}C_d Re_p \frac{\mu_f}{\rho_p d_p^2}\left(v_f - v_p\right) \quad (5)$$

where Re_p is the Reynolds number of the particles. The phase-to-phase resistance $K_{DPM}\left(v_p - v_f\right)$ can be defined as follows:

$$\mathrm{K_{DPM}}\left(\mathrm{v_p} - \mathrm{v_f}\right) = \sum\nolimits_{\mathrm{i}=1}^{\mathrm{N}} \mathrm{m_i F_D}\left(\mathrm{v_f} - \mathrm{v_p}\right)/\mathrm{V_{cell}} K_{DPM}\left(v_p - v_f\right) = \sum\nolimits_{i=1}^{N} m_i F_D\left(v_f - v_p\right)/ V_{cell} \quad (6)$$

where $N = N_p \cdot N_{Pracel}$ is the total number of particles in a cell, m_i is the mass of particle i, and v_{pi} is its velocity.

The solution of the above DDPM model still depends on the coupled framework of CFD-DEM. The coupling principle of CFD-DEM is presented in Fig.2

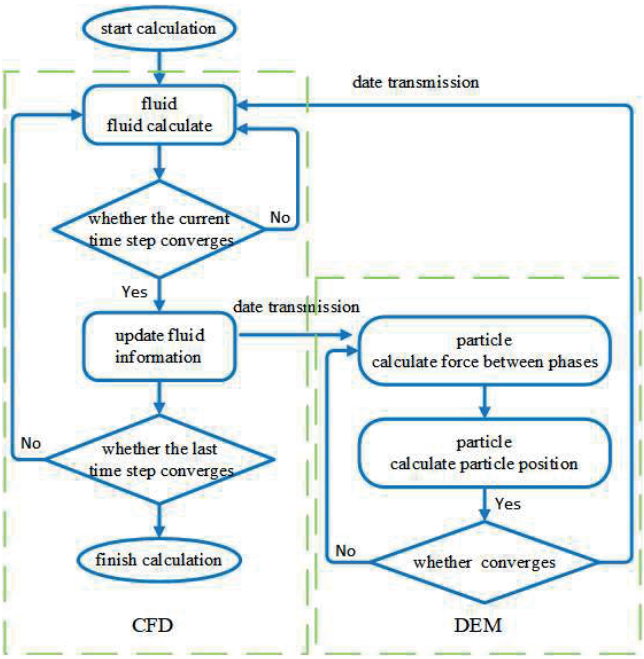

Fig.2 CFD-DEM coupling principle

In each time step, the CFD solver calculates the continuous phase flow until the calculation iterates to convergence. Then the fluid conditions of the grid element are transferred to the DEM solver to calculate the force on the particles and to solve the particle position, velocity and other parameters of particle motion. After the iterative calculation of DEM is completed, the information in the calculation element is estimated and fed back to the CFD solver together with the interphase forces. The CFD solver uses this data to solve the continuous-phase flow field, updates the flow region, and cycles into the next time step. Finally, stable and reliable particle field information can be obtained until the two fields converge.

B. Physical model and meshing

In order to explore the coupling mechanism of the multiphase flow, the following structure of a jet nozzle is selected as a computational domain, with its geometry shown as Fig.3. The simulation domain is constructed by a solid liquid inlet section, a high-pressure water inlet, an annular chamber from which emerge, 4 nozzles, a mixture chamber and an outlet section. Considering the possible influence of backflow at the inlet and outlet positions, the inlet section and outlet section are extended by 3 pipe diameters. The physical dimensions of the model are as follows: the diameter of solid -liquid inlet section is 7 mm, the diameter of the high-pressure water inlet is 15 mm, the nozzle outlet diameter

is 0.65 mm, and the outlet diameter was 6 mm. The particle diameter is 0.2mm and the jet device operates at standard atmospheric pressure.

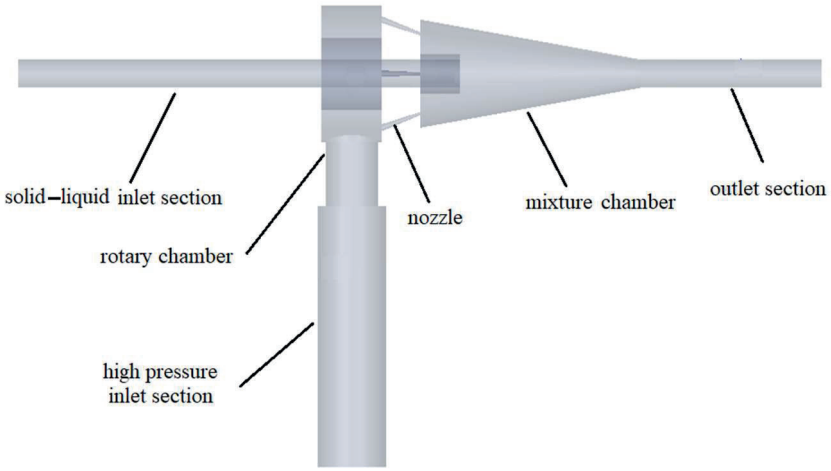

Fig.3 Geometric model of jet device

The 3D model of the fluid domain was imported into the ICEM software for computational meshing. An unstructured grid with excellent adaptability is used to model the complex domain, and the grids of the nozzles and the grids of the nozzles were refined. In this paper, four types of grids with different number of nodes were tested. As shown in Fig.4, the flow rate of the solid-liquid inlet pipe is simulated and relative error between numerical calculation and experimental results are obtained, verifying the grid independence. When the total number of mesh elements exceeds 220,000, the flow rate error is within 3%. The final total number of fluid domain mesh elements is 227037, as presented in Table 2.

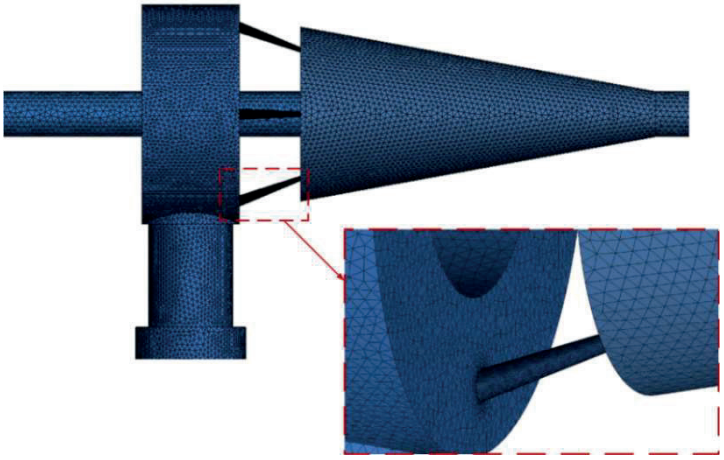

Fig.4 Computational Grids

Table 2

Grids independence analysis

Grid grades	Grids Number	Flowrate (kg/s)	Relative error
Type 1	89015	0.526	5%
Type 2	146620	0.521	4.2%
Type 3	170854	0.517	3.4%
Type 4	227037	0.515	3%
Experiment		0.53	

C. Boundary conditions and numerical procedure

The particles and device wall are metal with a density of 7800 kg/m^3, Poisson′s Ratio 0.3, Shear Modulus of 7×10^7 MPa. The Coefficient of Restitution and Rolling friction are 0.5 while the rolling friction coefficient is 0.01 among particles as well as particles with walls. The particles involved in this paper are iron grits with a diameter of 0.2mm. The boundary conditions in this paper were: the two inlets where velocity inlet with the solid-liquid inlet velocity was 11.8m/s, the feeding fluid inlet velocity was 4m/s. The outlet was standard atmospheric pressure. The rates of mass flow were 0.8 kg/s, 0.5 kg/s, and 0.3 kg/s, respectively (assuming that the two fluids had mixed uniformly). The total calculation time was 0.22s, while the time step for fluid was 1×10^{-4} s. Since the particle time step must be less than the fluid time step, the time step of particles was set as 5×10^{-5} s. The k-ε model and standard wall boundary were adopted in this turbulence model. Additionally, Hertz-Mindlin with Archard Wear model were used for predicting the wear of the jet device.

3. EXPERIMENTAL VALIDATION

The test rig for the jet device is shown as Fig.5. The red pipeline is the flow of iron grits and water, the blue one is the feeding liquid inlet pipeline. The slurry pump in black line conveys the particles back to the mixing tank, which is equipped with an agitator to ensure the uniformity of particles and water. Considering the operating risks from high pressure and high speed within the nozzle, the pressure of the feeding fluid and flow rate of the transported media are measured in the experiment, not the details of the multiphase flow inside the jet domain.

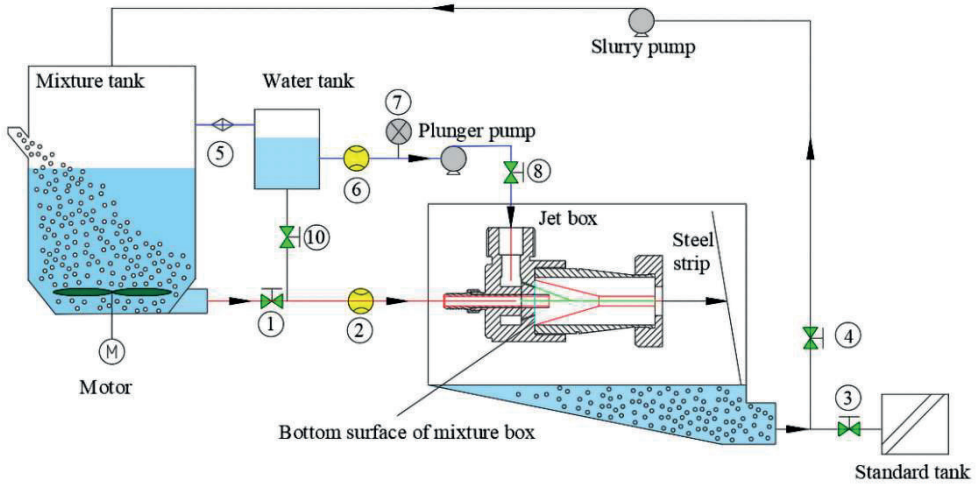

① valve1 ② flowmeter1 ③ valve 2 ④ valve3 ⑤ filter screen ⑥ flowmeter 2 ⑦ pressure gauge1 ⑧ valve4 ⑨ valve5 ⑩ pressure gauge2

Fig.5 Schematic diagram of the test device

The accuracy and range of the electromagnetic flowmeter were respectively ±0.3%, 0~15m/s, while those of the pressure gauges were ±0.2%, and the range was 0~60Mpa. The particles in the experiment were spherical iron grits. The mass concentration of particles in the mixture tank was 70%. In the test, the speed of the plunger pump was controlled to obtain various outlet pressure: 30 MPa and 50 MPa. The corresponding parameters of high-pressure water flow and ejection solid-water slurry were given in Table 3. The relative errors between the actual and simulated mass flow rate under the conditions of 50Mpa and 30Mpa were 5.8% and 5.4% respectively, which illustrated that the method was able to capture the gross flow behaviors in the nozzle.

Table 3

Solid-liquid jet test parameters

Outlet pressure of Plunger pump	Mass of high-pressure water	Iron grit mass (test)	Iron grit mass (CFD)	Error (%)
50 MPa	22 L/min	68 kg/min	72 kg/min	5.8
30 MPa	18 L/min	37 kg/min	39 kg/min	5.4

4. RESULTS ANALYSIS

In order to reveal the solid-liquid two-phase flow characteristics of the jet device, this paper examines it from the viewpoint of flow structure, particle motion, jet characteristics and particle impact on the wall.

A. Flow appearances and structures

The pressure and velocity are important parameters that characterize the flow profiles. Fig.6 shows the static pressure and streamline in the middle section of the device. The pressure begins to drop rapidly at the discharge end of the nozzle and rises to a certain extent at the middle section of the mixing chamber. Then it starts to drop again, as shown in Fig. 6(a). The two most obvious positions of the pressure drop are the nozzle outlet and the throat of the jet, that is, the connection between the mixing chamber and the outlet section. The pressure drop gradient in the direction of high-pressure water flow is significantly greater than that of the two-phase flow of the conveyed medium. There are three main stages in the jet region: suction zone of transported fluid, two-phase flow mixing zone, and dissipation zone of outflow. Fig. 6(b) indicates the velocity contour and streamlines. The two-phase fluid begins to enter the domain and mix with the feeding fluid from the outlet of the nozzles, then their velocity gradually increases till the outlet of the jet domain. It should be noted, that the motion in the mixing zone is asymmetrical and this is due to the asymmetry of the high-pressure jet flow upstream and the rapid shrinkage of the cross sections in the flow direction, leading to a significant vortex forming at one side. It will be shown that this vortex has a strong effect on particle retention and surface wear.

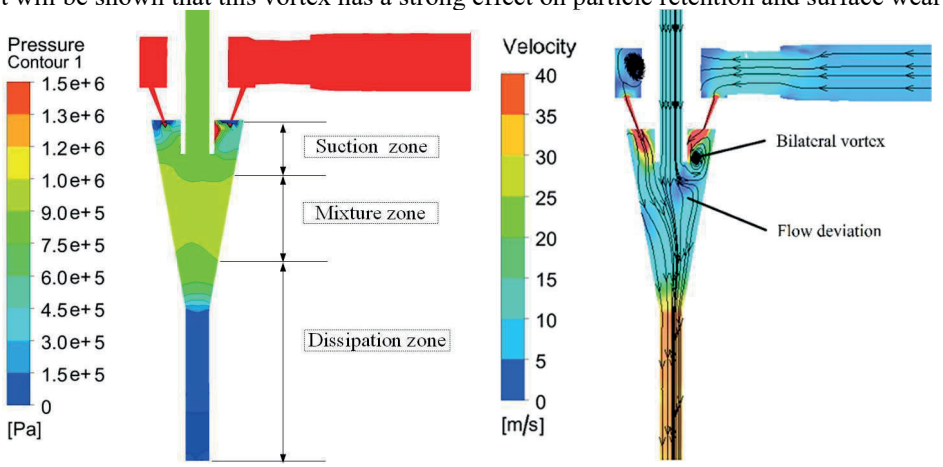

(a) Pressure distribution (b)velocity and streamlines distribution

Fig.6 Pressure and streamlines distribution in the middle section

B. Particles movement characteristics

Fig.7 indicates the spatial distribution and velocity characteristics of particles in the mixture chamber. The two-phase flow diffuses rapidly after mixing with the feeding fluid. A small part of the particles migrates to the bilateral chamber, and most particles generate a high-speed area near one side of the middle. At the outlet of the mixture chamber, the particles and water are mixed evenly, which ensure the effectiveness of flushing and dust removal. According to Fig.7 the migration of particles in the mixture chamber are complex in the process of mixing and diffusion. Despite this, the movement of the particles can be divided into two categories, dispersed flow and mainstream flow. The dispersed flow are the particles affected greatly by high pressure water, while mainstream flow is mainly the particles that are uninfluenced by the high-pressure water. This is because the mainstream particles are located in the middle of the transported two-phase flow, so they are less affected by the high-pressure water. Conversely, the dispersed flow outside the main two-phase flow is directly in contact to high-pressure water and carries out significant energy exchange. The corresponding particle's velocity's magnitude and direction are dramatically changed.

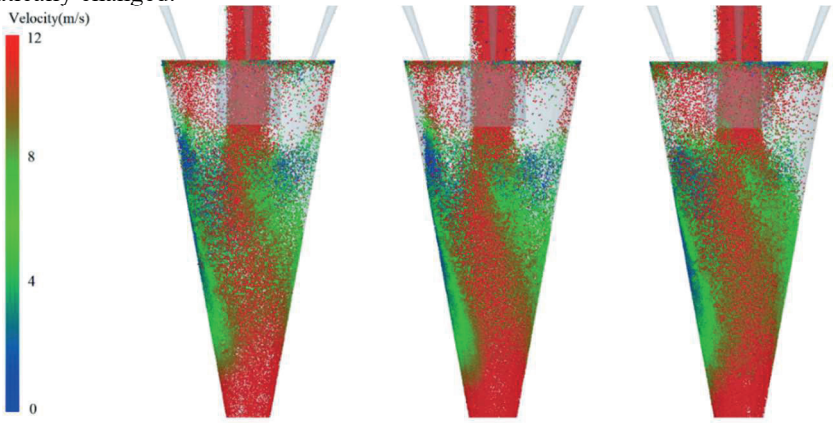

Fig.7 Spatial distribution of particles

Two types of representative particles, A and B are extracted from the dispersed flow and the mainstream flow respectively. The motion trajectories of the two particles are shown in Fig.8 (a) and (b). The trajectory of particle A is more complex than particle B in the mixture chamber. Particle A migrates to the bottom surface of the mixture chamber after contact with the high-pressure water, which produces wear through the changes of the particle's velocity direction and magnitude. Finally, particle A follows most of the other particles to merge and flow out along the main flow direction, where it collides with the wall again. It can be seen that there are many collisions among the particles and bottom surface of the mixture chamber, which produces serious damage. Particle B, is located at the centre of the inlet of the solid-liquid two phase flow and simply goes out from the outlet after a slight fluctuation in the main flow direction in the mixture chamber. There is no

contact and collision with the wall during the whole process. Fig.8 (c) and (d) present the trend and magnitude of the circumferential velocity V_C and the radial velocity V_Z of particle A and B which are relatively consistent from the inlet to the outlet section. The motion is mainly limited by the constraints of the walls on both sides, so the particle behavior tends to be unified. The V_Z of Particle A and B increase again in the outlet section due to the conversion of pressure energy.

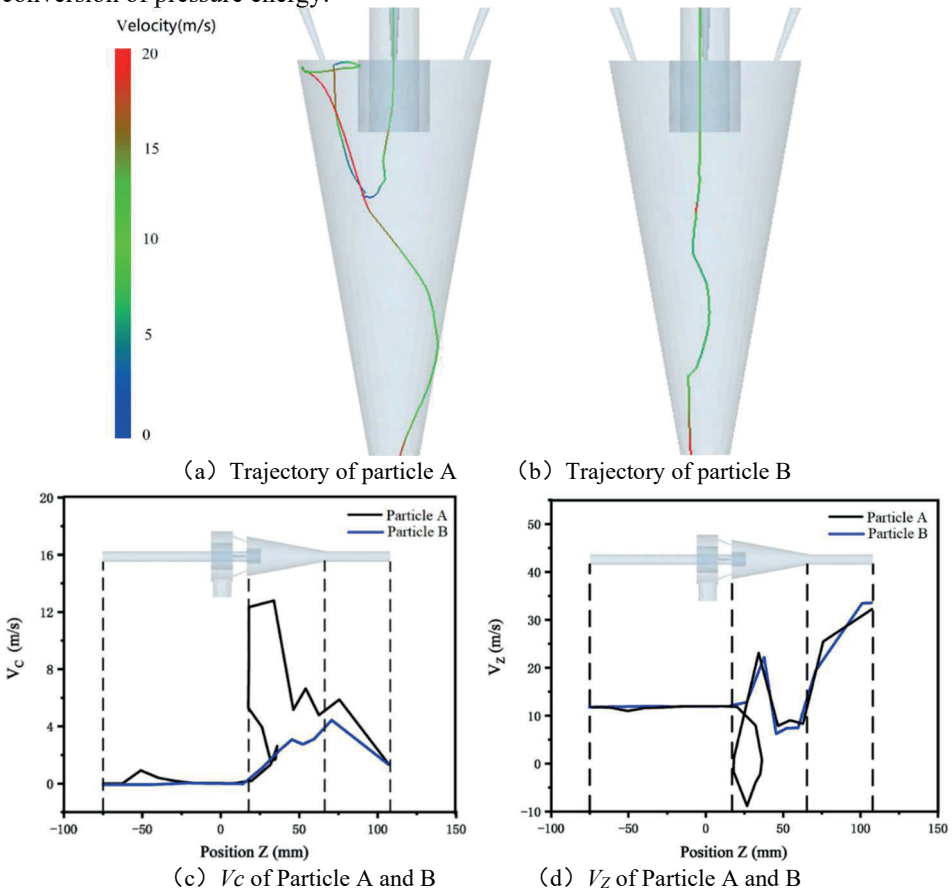

（a）Trajectory of particle A （b）Trajectory of particle B

（c）*Vc* of Particle A and B （d）V_Z of Particle A and B

Fig.8 Motion trajectories of particle A and B

C. Characteristic analysis of jet

In order to capture the temporal and spatial changes of the flow parameters in the jet, this paper selects the jet path of high-pressure water and the motion path of the solid-liquid flow as variables shown in Fig.9 to investigate the pressure and velocity changes at different spatial positions.

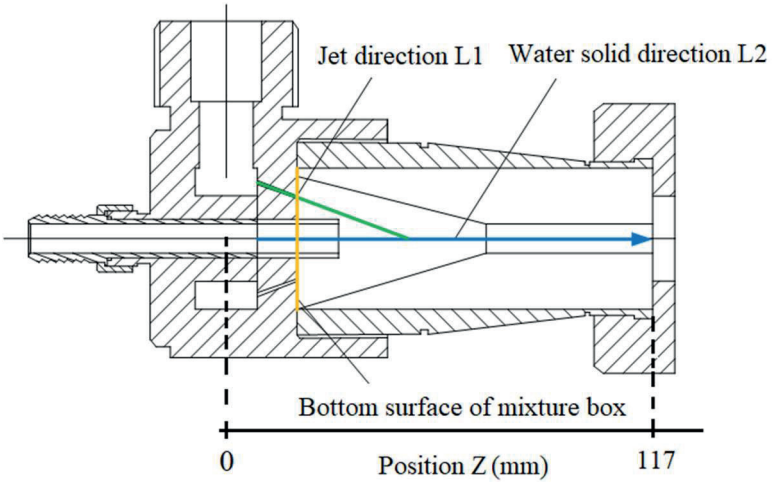

Fig.9 Identification of jet and slurry path

Fig.10 shows the velocity and pressure change curves in the jet direction L1 and the horizontal direction L2 under three mass flow conditions of 0.3kg/s, 0.5kg/s, and 0.8kg/s for the two-phase flow. Fig.10 (a)and (b) indicate that the flow velocity and pressure changes in the direction of L1 under three working conditions are highly consistent. First, the velocity in the nozzle increases rapidly and the maximum value 421m/s appears before the high-pressure water enters the mixture chamber. The velocity drops sharply when entering the mixture chamber and stops until mixing with the iron grits. There is a rapid drop of pressure in the same position. The trend of pressure and velocity in direction L2 under three working conditions is also similar (Fig.10c and 10d). When the mass flow is 0.8kg/s, the pressure and velocity are almost the maximum. The pressure keeps stable in the inlet section, then drops to almost 1 atm at the outlet. Alternatively, the velocity of particle decreases slightly at first, then increase at the outlet and stay at 35~40m/s. The reason for the growing velocity of water in direction flow L2 is mainly that the energy of high-pressure water in jet direction L1 is transferred to water and particles in direction flow L2. The pressure and velocity stabilize after mixing.

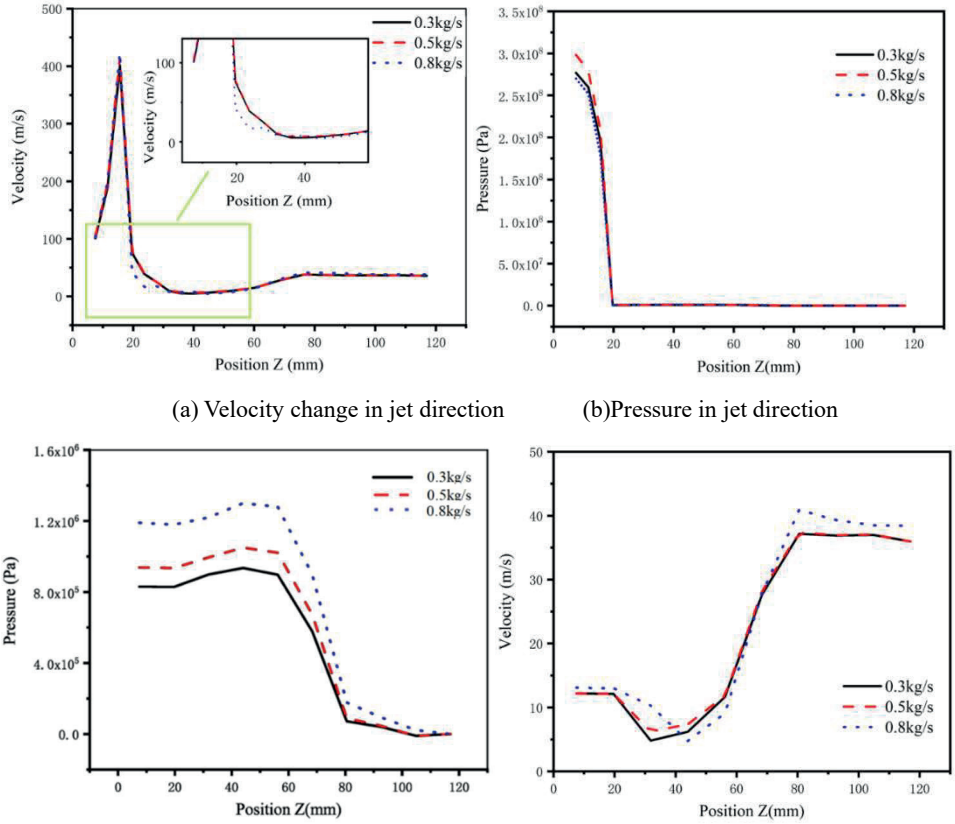

(a) Velocity change in jet direction (b)Pressure in jet direction

(c)Pressure of slurry in the direction of flow (d) Velocity of slurry in the direction of flow line

Fig.10 Variation characteristics of pressure and velocity along the path of jet and slurry

D. The particle impact on bottom of mixture chamber

Fig.7 and Fig.8(a) clearly show that collisions exist between particles and the bottom of the mixture chamber. In actuality, the wear on the bottom surface is a very serious problem. It is important to analyze the mechanism of wear formation and reduce ict. Fig.11 indicates the number of collisions, average normal force and tangential force on the bottom surface of the mixture chamber in the time period of 0~0.22s. Number of collisions is basically stable and fluctuates regularly in a certain range with time. The number of collisions is the maximum when the particle mass flow is 0.8kg/s. It can be seen from Fig.11(b) and (c) that after entering the stable state, the normal and tangential force show time-varying pulsation. The normal force is significantly greater than the tangential force under three different working conditions. The fluctuation range of tangential force is consistent under three working conditions, and the fluctuation range of normal force

increases with the increase of particle mass flow. The pulsation process may result from the turbulence irregularity of the water movement in the nozzle, which makes the velocity of water pulsating.

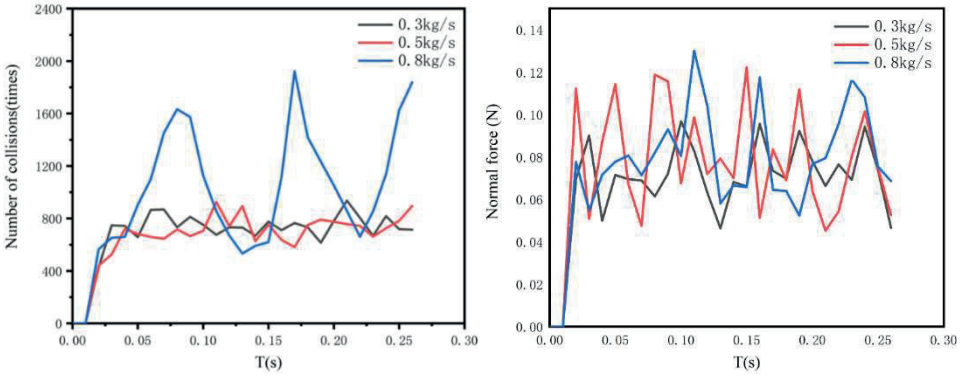

(a) Number of collisions on the bottom surface of mixture box (b) Average Normal Force

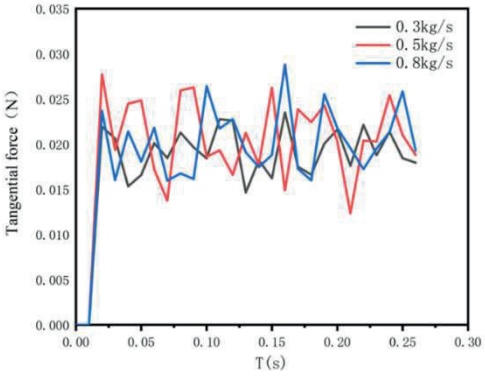

(c) Average tangential force

Fig.11 Particle action on the horizontal wall

Fig.12 shows the predicted average wear thickness and wear rate of particles on the bottom surface of the mixture chamber. The curve of average wear thickness increases linearly. By analyzing the corresponding average wear rate, the process can be divided into three stages as indicated in Fig.12: single phase flow stage (stage I); mixing stage (stage II); stable stage (stage III). In stage I, particles have not contacted the bottom surface of the mixture chamber. With a large number of particles entering the mixture chamber and continuously mixing with the high-speed water flow, more and more particles reach the bottom surface and collide with it. Then the wear rate grows rapidly as shown in stage II. In stage III, the particle wear rate enters the slow increasing area near 0.075s and reaches a steady state at 0.175s. Stage II and stage III take up merely a small part of the whole time. The last wear rate is 9.29×10^{-4}mm/s.

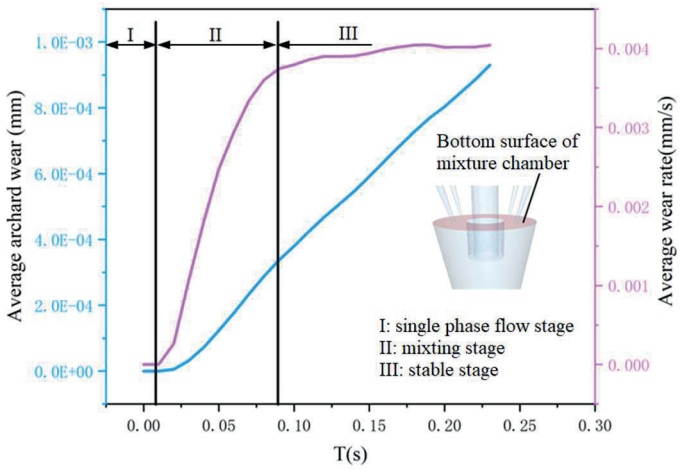

Fig.12 Average Archard wear and Average wear rate on the horizontal wall

5. CONCLUSIONS

In this paper, an optimized DDPM model which considers the interaction between the liquid phase and the particle is applied to investigate the particle's movement, flow field mechanism and wear characteristics. The following conclusions are obtained:

1. The method combining the DDPM model and the discrete element technique is capable of describing the dense particle two-phase flow field. Details of flow field which show obvious pressure gradients in the mixture chamber were obtained. The flow path deviates to a certain extent after the two-phase flow mixed with feeding fluid. There is an obvious recirculating flow at one side of the mixture chamber.

2. The spatial distribution and migration characteristics of the particles are roughly consistent with the motion of the flow field which proves that the particles follow the water well. There are mainly two forms of movement in the mixture chamber: the main flow and the dispersed flow. Particles in dispersed flow have complex trajectory owing to particle wall collisions.

3. Changes in the pressure and velocity of flow across three conditions considered were similar and were complex in the directions of the jet and the transported fluid. The energy of the feeding fluid was transferred to the transported liquid in the mixture chamber. Finally, the velocity and pressure of flow became stable in the outlet section of the device

4. The force on the wall and the collision of particles indicate time-averaged pulsation. The wear of the wall is roughly divided into three stages: single phase flow stage (stage I); mixing stage (stage II); stable stage (stage III). Stage I and stage II take up a small part of the whole time. The final steady state wear rate is 9.29×10^{-4}mm/s.

5. In future work, the influence of the impact velocity of the particles, the impact angle and the spatial distribution on the wear rate will be studied in depth.

REFERENCES

1. Adamczyk W.P., Kozołb P., Węcel G., Klimanek A., Białecki R.A. Czakiert T., "Modeling oxy-fuel combustion in a 3D circulating fluidized bed using the hybrid Euler–Lagrange approach," Applied Thermal Engineering **71**, 266 (2014).
2. Adnan M., Sun J., Ahmad N., and Wei J., "Comparative CFD modeling of a bubbling bed using a Eulerian–Eulerian two-fluid model (TFM) and a Eulerian-Lagrangian dense discrete phase model (DDPM)," Powder Technology 383, 418 (2021).
3. Ayeni O., Tiwari S., Wu. C., Joshi J.B., and Nandakumar K., " Phys Fluids (2020) **32**, 073304 (2020).
4. Axinte D.A., Karpuschewski B., Kong M.C., Beaucamp A.T., Anwar S., Miller D., and Petzel M., "High Energy Fluid Jet Machining (HEFJet-Mach): From scientific and technological advances to niche industrial applications," CIRP Annals **63**, 751 (2014).
5. Chen F., Miao X., Tang Y., and Yin S., "A review on recent advances in machining methods based on abrasive jet polishing (AJP)," The International Journal of Advanced Manufacturing Technology **90**, 785 (2016).
6. Chen X., and Wang J, "A comparison of two-fluid model, dense discrete particle model and CFD-DEM method for modeling impinging gas–solid flows," Powder Technology **254**, 94 (2014).
7. Du M., Wang H., Dong H., Guo Y., and Ke Y., "Numerical research on multi-particle movements and nozzle wear involved in abrasive waterjet machining," The International Journal of Advanced Manufacturing Technology **117**, 2845 (2021).
8. Guo R., Zhou C., and Yuan S., "Influence of Abrasive Water Jet Parameters on Steel Surface," Jom **72**, 4273 (2020).
9. Hou R., Huang C., and Zhu H., "Experimental study on pulsation behavior of the ultrasonic vibration-assisted abrasive waterjet," The International Journal of Advanced Manufacturing Technology **91**, 3851 (2017).
10. Huang F., Mi J., Li D., Wang R., and Zhao Z., "Comparative investigation of the damage of coal subjected to pure water jets, ice abrasive water jets and conventional abrasive water jets," Powder Technology **394**, 909 (2021).
11. Jagadish, G.C., Manjunath P., Tatjana.V.S., Jabir. M., and Zhang L., "Abrasive water jet machining for a high-quality green composite: the soft computing strategy for modeling and optimization," Journal of the Brazilian Society of Mechanical Sciences and Engineering **44**, (2022).
12. Li S., and Shen Y., "Multi-fluid modelling of hydrodynamics in a dual circulating fluidized bed," Advanced Powder Technology 31, 2778 (2020).
13. Liu X., Su J., Qian Y., Cui L., and Liu X., "Comparison of two-fluid and discrete particle modeling of gas-particle flows in micro fluidized beds," Powder Technology **338**, 79 (2018).
14. Lv Z., Hou R., Tian Y., Huang C., and Zhu H., "Investigation on flow field of ultrasonic-assisted abrasive waterjet using CFD with discrete phase model," The International Journal of Advanced Manufacturing Technology **96**, 963 (2018).
15. Mokso R.B.R., Narayanan C., Weiss D.A., and Heiniger K.C., "Ultra-fast X-ray particle velocimetry measurements within an abrasive water jet," Experiments in Fluids **54**, (2013).
16. Ostermeier P., DeYoung S., Vandersickel A., Gleis S., and Spliethoff S., "Comprehensive investigation and comparison of TFM, DenseDPM and CFD-DEM for dense fluidized beds," Chemical Engineering Science **196**, 291 (2019).
17. Patro P., and Dash S.K., "Two-fluid modeling of turbulent particle–gas suspensions in vertical pipes," Powder Technology **264**, 320 (2014).

18. Qiang Z., Wu M., Miao X., and Sawhney R., "CFD research on particle movement and nozzle wear in the abrasive water jet cutting head," The International Journal of Advanced Manufacturing Technology **95**, 4091 (2018).
19. Shi B., Pan J., Wu L., Zhang X., Qiu Y., Zhang Y., and Xu J., "A Prediction Method of Wear for Volute Casing of a Centrifugal Slurry Pump," Geofluids **2020**, 1 (2020).
20. Wu C., Cheng Y., Ding Y., and Jin Y., "CFD–DEM simulation of gas–solid reacting flows in fluid catalytic cracking (FCC) process," Chemical Engineering Science **65**, 542 (2010).
21. Zhao R., Zhou Y., Zhang D., and Gao X., "Numerical investigation of the hydraulic transport of coarse particles in a vertical pipe based on a fully-coupled numerical model," International Journal of Multiphase Flow 155, (2022).